Volume 16, Number 5, 2023. pp. 579-585

Jordan Journal of Physics

ARTICLE

Voigt Profile is Suitable for Impedance Spectroscopic Analysis of BLSF Ceramics

Md. Abdul Basheer[a], **Md. Samdani**[b], **Syed Tahseen Hussain**[a] and **N.V. Prasad**[c]

[a] *Deccan College of Engineering & Technology, Hyderabad, India.*
[b] *Engineering Department, University of Technology and Applied Science, Salalah, Sultanate of Oman.*
[c] *Material Research Laboratories, Department of Physics, Osmania University, Hyderabad 500007, India.*

Doi: https://doi.org/10.47011/16.5.8

Received on: 23/01/2022; *Accepted on: 14/04/2022*

Abstract: In our earlier studies, samarium-modified bismuth layer-structured ferroelectrics (BLSF), namely Sm_xBi_{3-x} $TiNbO_9$ (SBTN); (x=0, 0.2, 0.4, 0.6. 0.8, and 1.0), prepared by solid-state reaction method, have shown broad dielectric relaxations. Among all the compositions, $Bi_{2.6}Sm_{0.4}TiNbO_9$ (BST-0.4) has shown a lower tolerance factor, high remnant polarization (Pr) value, and low stretching factor. In addition, the compound has shown interesting broad dielectric relaxation and non-Debye nature. The specific reasons for the broad relaxation remain unclear. To gain more insights, we synthesized multi rare earth ion substituted compounds, namely, $Bi_{2.6}La_{0.2}Sm_{0.2}TiNbO_9$ (sample A) and $Bi_{2.6}La_{0.2}Gd_{0.2}TiNbO_9$ (sample B), using the conventional solid-state reaction method. A single impedance spectroscopic approach alone may not be sufficient to explain the asymmetric or non-Debye behavior, therefore Lorentzian, Gaussian, and Voigt fitting were adopted in the present investigation. From the analysis, the Voigt profile (V_f and V'_f) is found to be a valuable alternative tool to understand the broad impedance non-Debye relaxations. Finally, results were corroborated by dc-conductivity data.

Keywords: BLSF, Modulus spectroscopy, Relaxation, Defect-mechanism, Gaussian, Lorentz and Voigt fitting, Dc conductivity.

Introduction

Advanced spectroscopic relaxation studies require the intensity and magnitude of the response function. The peaks observed in the spectrum provide insights into the different relaxation species present within the composition. A recent report states that the Gaussian–Lorentzian sum/product functions play a role in the analysis of x-ray photoelectron spectroscopy [1-3]. In addition, the Voigt function and its derived parameters have shown accurate results in mathematical expansion relations [4]. Our recent report on the Voigt analysis on impedance spectroscopic peaks gives information about the interaction or competitive interaction of both long-range and short-range ordering [5]. It is a known fact that the simple broad impedance spectroscopic peak explains only the fundamental description of single or multiple ion relaxation (non-Debye) phenomena. However, to explore the complete picture of relaxation, an advanced mathematical approach is necessary. It has been reported in the literature that the broadening of the spectroscopic peaks can be described either by Gaussian or Lorentzian fitting [6, 7].

Corresponding Author: Md. Abdul Basheer **Email**: baseer.abdul7@gmail.com

It is pointed out that more or less bell-shaped frequency response curves (shown in Fig. 1) theoretically can be fitted with Lorentzian L(x) and Gaussian G(x) curves. If the experimental curves fit with the Voigt profile, then one can propose a criterion based on the peak value and FWHM. The same criterion is applicable to advanced spectroscopic data. Moreover, the FWHM of the Voigt profile along with its parameters has a low signal-to-noise ratio [8, 9].

The Voigt function is considered particularly significant for representing the symmetric features of any respond peak profile due to its theoretical importance and practical suitability for fitting into peaks of experimental data [5-7, 10]. It is a known fact that the impedance spectroscopic plots show relaxation peaks in the radio frequency region, corresponding to the different relaxing species that are present in the composition. Generally, the dielectric relaxation peaks give information about the competitive interaction of both long-range and short-range ordering that are present in the sample. The same information can be extracted from the specified peak shape and its width [11]. Spectroscopic peaks are generally described either by Gaussian or Lorentzian fitting [6, 12]. The former explains the single relaxation, and the latter describes multiple relaxation phenomena. In addition, it provides information about the instrumental limitations.

The Voigt function (V(x)) is defined as the convolution between Lorentzian (L(x)) and Gaussian function (G(x)), expressed as

$$(V(x) = G(x) \oplus L(x)) \quad (1)$$

The Voigt function can interpret the data in twofold: (i) graphical point of view, (ii) numerical point of view. Ida *et al* [7] pointed out that the Gaussian width and the parameter (a) give an asymptotic explanation for dielectric relaxation data. Here, the parameter (a) is defined as the ratio of Lorentzian and Gaussian full width at half maxima (FWHM). Many researchers adopted Voigt fitting to resolve the overlapping line shapes of different modes of Raman spectra [13-15].

To explore the distinctive characteristics and gain deeper insights into non-Debye type, multivalent rare-earth ion-doped materials, namely, $Bi_{2.6}La_{0.2}Sm_{0.2}TiNbO_9$ (sample A) and $Bi_{2.6}La_{0.2}Gd_{0.2}TiNbO_9$ (sample B) were prepared. In addition, intergrowth of A and B (sample C) and solid-solution of A and B (sample D) were synthesized. This investigation focuses on studying the true line intensity and shape of spectroscopic data, considering instrumental distortion, by means of Lorentzian and Gaussian functions. Combined analyses of this nature, especially in the context of BLSF, are limited in the existing literature.

In the present study, the real and imaginary parts of the modulus (complimentary to dielectric data) are calculated by using the following equations:

$$M' = \frac{\varepsilon'}{\left(\varepsilon'^2 + \varepsilon''^2\right)} \quad (1)$$

$$M'' = \frac{\varepsilon''}{\left(\varepsilon'^2 + \varepsilon''^2\right)} \quad (2)$$

Where ε' *and* ϵ" represent real and imaginary part of permittivity, respectively. The complex modulus response function (M*) can be described as the combination of both real and imaginary parts of the modulus, i.e., $M^* = M' + iM'' = j\omega C_o Z^*$. Here, Z* represents the complex impedance function. The obtained imaginary part of modulus data (M") is plotted against frequency. The data is fitted with Gaussian, Lorentzian, and the Voigt functions for all the samples. Finally, the results are corroborated by the ac-conductivity data.

Experimental Methods

$Bi_{2.6}Sm_{0.4}TiNbO_9$ (BST-0.4), $Bi_{2.6}Sm_{0.2}La_{0.2}TiNbO_9$ (BSLT, sample A), $Bi_{2.6}Gd_{0.2}La_{0.2}TiNbO_9$ (BGLT, sample B), single phase ceramics were prepared by the solid-state route. In addition, intergrowth (x BSLT - (1-x) BGLT, where x = 0.49, sample C) and solid solution (BSLT – BGLT, sample D) ceramics were prepared. Detailed synthesis and the lattice parameters were described elsewhere [11, 16]. The impedance measurements were made by Hewlett-Packard (HP4192A) impedance analyzer.

Results and Discussions

The Lorentz and Voigt equations are given in the following expressions:

$$Y = Y_0 + \left(\frac{A}{w \times \sqrt{\frac{\pi}{2}}}\right) \times exp\left(\frac{-2((x-x_c)}{W}\right)^2$$

(Gaussian) (3)

$$Y = Y_0 + (2 \times \frac{A}{\pi}) \times \left(\frac{w}{(4\times(x-x_c)^2+W^2)}\right) \quad \text{(Lorentz) (4)}$$

$$Y = Y_0 + \left(\frac{A\times 2\times \ln(2)\times w_L}{\pi^{1.5}\times {w_G}^2}\right) \times \int \frac{\exp(-t^2)}{\left(\sqrt{\ln(2)}\times\frac{w_L}{w_G}\right)^2} + \left(\sqrt{4\times\ln(2)} \times \frac{(x-x_c)}{w_G - t}\right)^2 \quad \text{(Voigt) (5)}$$

Here, Y_0 is the offset value, A is the area under the curve, W is the width of the curve, and X_c is the center of the peak position. The Gaussian and Lorentzian parameters, w_G and w_L, are related to the FWHM of Gaussian ($\acute{\Gamma}_G$), Lorentzian ($\acute{\Gamma}_L$), and [17]. The peak area, width, and peak position were also obtained by fitting the Voigt function, using Eq. (5). More information on the analysis is provided in our earlier paper [5].

The Voigt profile is defined as the convolution of the Gaussian and Lorentzian functions with FWHM values of Γ_G and Γ_L, and can be expressed as

$$f_v(x:\Gamma_G,\Gamma_L) = \left(\frac{2}{\Gamma_G}\right)\left(\frac{\ln 2}{\pi}\right)^{1/2} K\left[2\,(\ln 2)^{1/2}.\frac{x}{\Gamma_G}, (\ln 2)^{1/2}\frac{\Gamma_G}{\Gamma_L}\right] \quad (6)$$

Where the Voigt function K(x,y) defined as $\frac{y}{\pi}\int_{-\infty}^{\infty} exp\left[\frac{(-t)^2}{y^2+(x-t)^2}\right] dt.$

The variable shape of the Voigt function K(x,y) is specified by a single parameter (y) and the defined parameter $\rho \equiv \frac{\Gamma_L}{\Gamma_L+\Gamma_G}$. It should be remembered that the pre-requisite condition is $\Gamma_G + \Gamma_L = 1$.

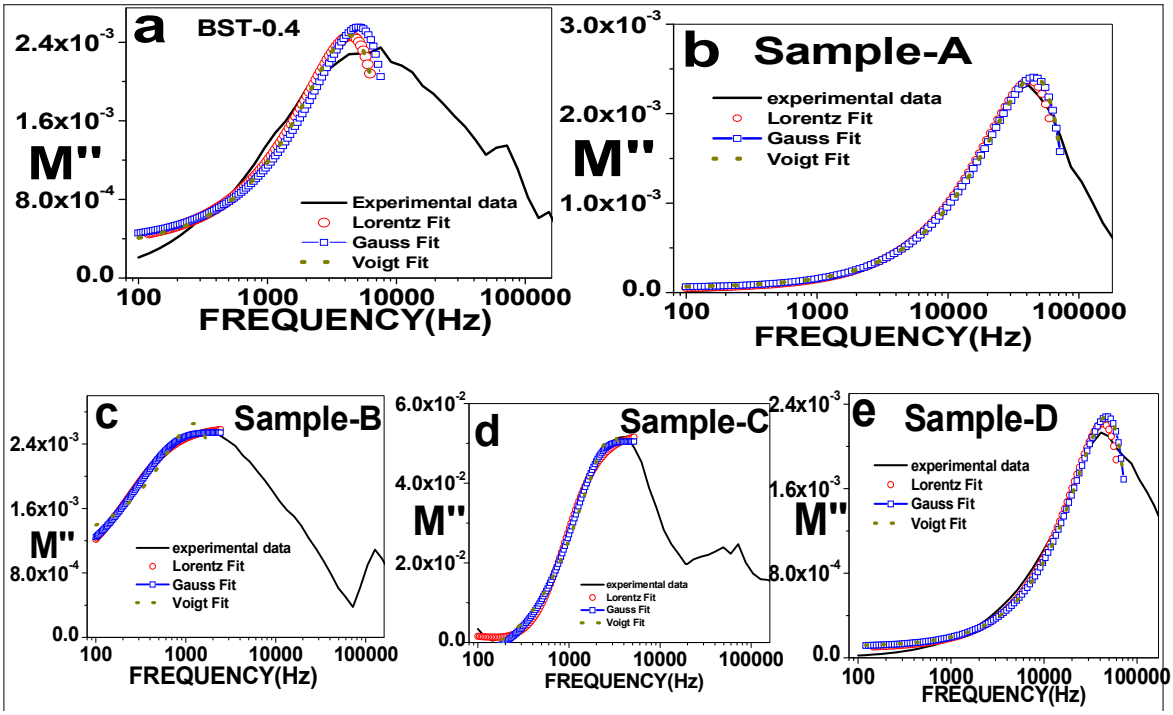

FIG. 1. Gaussian, Lorentzian, and Voigt fittings for (a) BST-0.4, (b) sample A, (c) sample B, (d) sample C, and (e) sample D.

Fig. 1 shows the variation of the imaginary part of the modulus with the frequency obtained at 450°C for all the samples, namely $Bi_{2.6}Sm_{0.4}TiNbO_9$ (BST-0.4), sample A, sample B, sample C, and sample D. The data is fitted up to the specified region, namely in the lower frequency range. The solid line represents the experimental data. The dotted and scattered lines represent theoretical data of Voigt, Lorentzian, and Gaussian fittings. The parameter values obtained from the fitting data (Fig. 1) are summarized in Table 1. Based on Fig.1, Voigt fitting is found to be the best fitting, compared to Lorentzian and Gaussian fittings. From the plot, a tentative conclusion is drawn that frequency determines the discrimination of the continuous (broad) peak and the augment. These types of curves explain the experimental data which are fitted by the Voigt profile. Based on the above consideration, Poppe and Wifers [18] defined the Voigt profile as:

$$f_v(x:\Gamma_G,\Gamma_L) = f_v(x:1-\rho,\rho)$$

$$f_v(x:\Gamma_G,\Gamma_L) = \left[\frac{1}{\Gamma_L+\Gamma_G}\right]\rho\left[\frac{x}{\Gamma_L+\Gamma_G};\rho\right] \quad (7)$$

TABLE 1. The parameters constructed based on the Gaussian, Lorentzian, and Voigt functions.

Temperature 450^{O}C Parameters → Samples	Function	Y_O	X_C	W	A	REDUCE $\chi 2$	Adj.R-Square
BST-0.4	Lorentz	-0.09678	4397.09016	59508.27762	9276.64193	2.12266E-8	0.96054
	Gaussian	-0.08773	5100.70902	46144.04324	5221.63805	3.58898E-8	0.93921
	Voigt	-0.07016	4375.78149	W_G 41963.90577 W_L 2.5441E-13	3244.28427	2.34264E-8	0.95847
Sample A	Lorentz	-0.06253	42007.98671	435655.75073	44412.16575	1.02546E-9	0.99836
	Gaussian	-0.065	45234.78241	339415.51961	28673.45483	4.02225E-9	0.99368
	Voigt	-0.0258	45208.37537	W_G 254893.22126 W_L 1.2893E-11	7656.98659	4.70385E-9	0.99261
Sample B	Lorentz	0.00261	-171.74573	535.9971	-2.37476	1.11394E-9	0.9949
	Gaussian	0.00254	-6158.83545	2702.20141	-200735.366 200735.36692 200735.366 200735.36692	1.01185E-9	0.99537
	Voigt	-0.04344	1228.44262	W_G 11288.10444 W_L 6.19819E-13	553.90439	1.36733E-8	0.93695
Sample C	Lorentz	0.05286	151.53198	1612.21115	-130.49574	1.11756E-6	0.99729
	Gaussian	0.05045	-808.81791	2426.46534	-216.24611	1.27828E-6	0.99675
	Voigt	-0.97014	2978.92071	W_G 20526.1362 W_L 9.10405E-14	22331.03341	3.91826E-6	0.98949
Sample D	Lorentz	-0.07326	42677.15288	501206.83254	59420.12424	3.80025E-9	0.99287
	Gaussian	0.07119	47368.16242	386212.07628	35565.81212	8.37619E-9	0.98495
	Voigt	-0.02973	47327.10101	W_G 296750.79938 W_L 1.11673E-11	10113.07777	9.28601E-9	0.98332

Fig. 2 shows the variation of the Voigt profile as a function of arbitrary values (x). Since the Voigt function is the combination of both Gaussian and Lorentzian functions, the following equation is evident.

$$f_v = \rho \times \acute{\Gamma}_G + \rho \times \acute{\Gamma}_L \quad (6)$$

From Eq. (6), the Voigt function profile can be approximated to the final experimental value, and therefore the following equation is more suitable for application. Based on the arbitrary values of $\acute{\Gamma}_G, \acute{\Gamma}_L$, the Voigt profile function (f_V) is derived and finally given in the following equation [18]. For different ρ values (ρ = 0.3,0.7 & 1.0.), the variation of the Voigt function with different arbitrary ρ values can be presented the following equation:

$$\boldsymbol{f_V}(\boldsymbol{x}; \acute{\Gamma}_G, \acute{\Gamma}_L) = \left[\frac{1}{\acute{\Gamma}_G + \acute{\Gamma}_L}\right] \times \boldsymbol{\rho} \times \left[\frac{x}{\acute{\Gamma}_G + \acute{\Gamma}_L}\right] \quad (7)$$

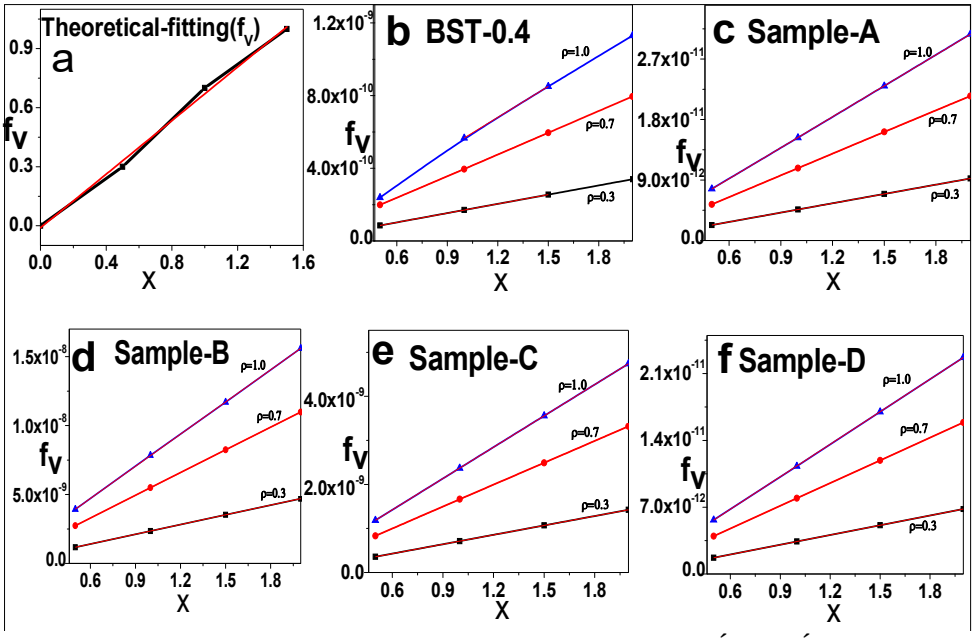

FIG. 2. Voigt profile as a function of augment and different ρ (values $\acute{\Gamma}_G$ and $\acute{\Gamma}_L$ are taken from Table 1).

By using the above equation f_V values were calculated for all samples, and the variation of f_V with x is shown in Fig. 3. From the plot, it is observed that f_V increases with the arbitrary parameter (ρ). The slope values were also found to increase with arbitrary values. The theoretical Voigt profile can be visualized by giving different ρ values and keeping the condition $\acute{\Gamma}_G + \acute{\Gamma}_L = 1$. The theoretical Voigt profile is shown in Fig. 2(a). The Voigt profile calculated for other samples for different ρ values is shown in Fig. 2(b)-2(f).

The variation of dc-conductivity with inverse temperature is shown in Fig. 3. The activation energies calculated from the slopes of the plot are depicted in Fig. 3. It has been reported in the literature that the oxygen vacancies were created due to the loss of bismuth ions at higher temperatures. These vacancies accumulated at the grain boundaries act as an opposite polarizing process. Hence, they may result in broad peaks near 450°C in all the samples [11, 16]. Moreover, the multiple rare-earth ionic incorporation at the bismuth site creates more vacancies on complex defect dipoles owing to the electron hopping process in singly or doubly ionized vacancies (Kroger-Vink reaction). The proposed defect formula for this compound is viewed as

$$Sm_{0.4}Bi_{2.6}TiNbO_9 = Bi_2O_3.2\left[Sm_{0.4}Bi_{0.6}[\,]_{1/2}Ti_{1/2}Nb_{1/2}O_3\right] \quad \text{(BST-0.4)} \quad (8)$$

$$Sm_{0.2}\,La_{0.2}Bi_{2.6}TiNbO_9 = Bi_2O_3.2\left[Sm_{\frac{0.2}{2}}La_{\frac{0.2}{2}}Bi_{\frac{0.6}{2}}[\,]_{1/2}Ti_{1/2}Nb_{1/2}O_3\right] \quad \text{(sample A)} \quad (9)$$

$$Gd_{0.2}La_{0.2}\,Bi_{2.6}TiNbO_9 = Bi_2O_3.2\left[Gd_{\frac{0.2}{2}}La_{\frac{0.2}{2}}Bi_{\frac{0.6}{2}}[\,]_{1/2}Ti_{1/2}Nb_{1/2}O_3\right] \quad \text{(sample B)} \quad (10)$$

$$Sm_{0.2}\,La_{0.2}Bi_{2.6}TiNbO_9 + Gd_{0.2}La_{0.2}\,Bi_{2.6}TiNbO_9 = 2Bi_2O_3.2\left[Sm_{\frac{0.2}{2}}Gd_{\frac{0.2}{2}}La_{\frac{0.4}{2}}Bi_{\frac{1.2}{2}}[\,]_{0.4/2}TiNbO_6\right] \quad \text{(samples C and D)} \quad (11)$$

Based on the defect formula mentioned above, fewer defects were seen in samples C and D compared to samples A and B. The results are consistent with the activation energy values depicted in Fig. 3.

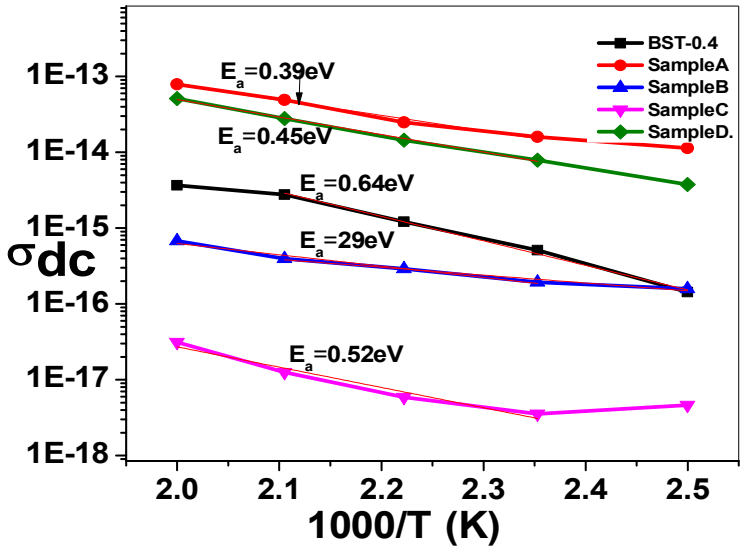

FIG. 3. The variation of σ_{dc} with 1000/T (K).

Many researchers have pointed out that Gaussian width is more important when compared to Lorentzian. However, the ratio between Gaussian and Lorentzian is <1. Several asymptotic expressions are adapted to analyze the data. In this connection, the Voigt profile seems to be more valid. In the Voigt profile, the parameters 'a' and 'b' are defined as

$a = \frac{W_L}{W_G}$ and $= \frac{x}{W_G}$, where W_L *and* W_G are related to $\acute{\Gamma}_L$ and $\acute{\Gamma}_G$.

From the above discussion, one can conclude that Voigt parameters a and b can be expressed as

$$\frac{b_{1/2}(a)}{a} = \frac{\acute{\Gamma}_V}{\acute{\Gamma}_L} = \sqrt{\ln 2}\,\frac{\acute{\Gamma}_V}{\acute{\Gamma}_G} \qquad (12)$$

And $\acute{\Gamma}_V \simeq \acute{\Gamma}_G \; \forall \; a \ll 1 \; \acute{\Gamma}_V \simeq \acute{\Gamma}_L \; \forall \; a \gg 1$

Based on the above equation, a, b, $b_{1/2}(a)$ values are calculated for all the samples shown in Fig. 4.

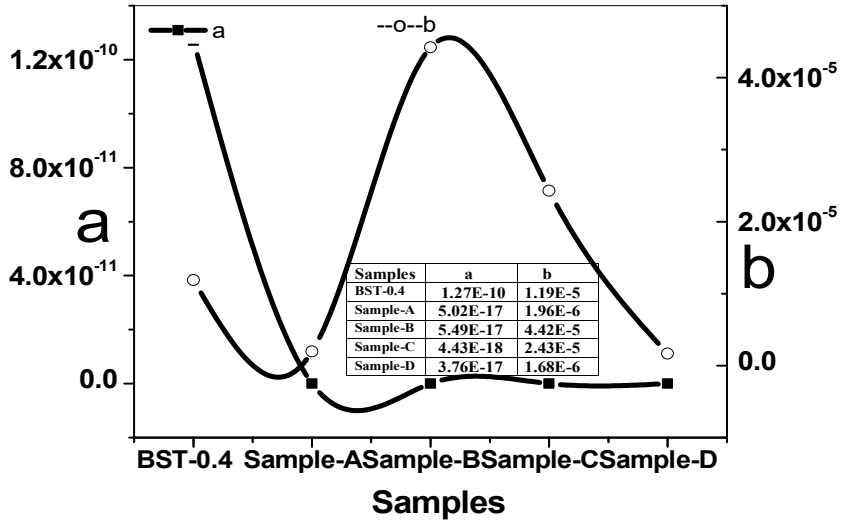

Samples	a	b
BST-0.4	1.27E-10	1.19E-5
Sample-A	5.02E-17	1.96E-6
Sample-B	5.49E-17	4.42E-5
Sample-C	4.43E-18	2.43E-5
Sample-D	3.76E-17	1.68E-6

FIG. 4. The variation of a and b values for all the samples.

The parameters 'a' and 'b' obtained from the fitting can be helpful in understanding the relaxation phenomenon. Parameter 'a' describes the Voigt profile and explanations the relaxation phenomenon. The relaxation is attributed to the presence of complex defect dipoles, where the defects (oxygen vacancies) combine with electrons to form complex dipoles. However, further studies are needed to speculate on the complete Voigt profile and complex defects.

Conclusion

The single impedance spectroscopic approach alone may not be sufficient to explain the asymmetric or non-Debye behavior. Therefore, a complete understanding of the relaxation requires an advanced mathematical approach. By adopting the complete Voigt profile, several conclusions can be drawn:

(i) Discrimination of the continuous (broad) peak and the function representing the augment function.

(ii) Parameters 'a' and 'b' obtained from the fitting may be helpful in understanding the relaxation phenomenon.

(iii) Parameter 'a' describes the Voigt profile and explains the relaxation phenomenon.

(iv) The relaxation phenomenon is attributed to the presence of complex defect dipoles, which is corroborated by the present study.

Acknowledgments

One of the authors (MAB) thanks the management of Deccan College of Engineering and Technology for the constant support and encouragement. The research work is partially financed by grants from the C-DST- PURSUE-11-2021programme, India.

References:

[1] Major, G.H., Fernandez, V., Fairely, N. and Matthew, R., Surf. Interface Anal., 54 (3) (2022) 262.

[2] Jain, V., Biesinger, M.C. and Linford, M.R., Appl. Surf. Sci., 447 (2018) 548.

[3] Westberg, J., Wang, J.Y. and Axner, O., J. Quant. Spectrosc. Ra., 113 (16) (2012) 2049.

[4] Mamedov, B.A., Mon. Not. R. Astron. Soc., 387 (4) (2008) 1622.

[5] Abdul Basheer, M.D., Prasad, N.V. and Prasad, G., IJSRPAS, 8 (2) (2020) 1.

[6] Rietveld, H.M., J. Appl. Cryst., 2 (1969) 65.

[7] Ida, T., Ando, M. and Toraya, H., J. Appl. Crystallogr., 33 (6) (2000) 1311.

[8] Alstrom Tommy, S., Mikkel, N.S., Tomas, R. and Anjana, B., Int. Conf. Acoust. Spee., (2017) 2317.

[9] Manani, N.H., Jethva, H.O. and Joshi, M.J., IJSRPAS, 08 (2020) 8.

[10] Langford, J.I., "Accuracy in Powder Diffraction II" Eds. Prince and J.K. Stalick (National Institute of Standards and Technology, Boulder, 1992), pp110-126.

[11] Abdul Basheer, M.D., Prasad, N.V., Prasad, G. and Kumar, G.S., B. Mater. Sci., 42 (2019) 1776-6.

[12] De Keijser, Th. H., Langford, J.I., Mittemeijer, E.J. and Vogels, A.B.P., J. Appl. Cryst., 15 (1982) 308.

[13] Sundius, T., J. Raman Spectrosc., 1 (5) (1973) 471.

[14] Rocco, H.O.Di., Iriarte, D.I. and Pomarico, J., J. Appl. Spectrosc., 55 (2001) 822.

[15] Weatherston, J.D., Worstell, N.C. and Wu, H.J., "Quantitative Surface-enhanced Raman Spectroscopy for Kinetic Analysis of Aldol Condensation Using Ag–Au Core–Shell Nanotubes", (The Analyst, 2016).

[16] Abdul Basheer, M.D., Gangadhar, V., Prasad, N.V., Prasad, G. and Kumar, G.S., J. Adv. Mater. Res., 1154 (2019) 80.

[17] Mahboob, S., Rizwana and Kumar, G.S., Integr. Ferroelectr., 167 (2015) 115-.

[18] Poppe, G.P.M.. and Wifers, C.M.J., ACM Trans. Math. Softw., 16 (1990) 38.